Draft version May 23, 2022
Typeset using LaTeX **twocolumn** style in AASTeX62



# Nonlinear Reconstruction of the Velocity Field

Yu Yu[1] and Hong-Ming Zhu[2,3]

[1]*Department of Astronomy, Shanghai Jiao Tong University, 800 Dongchuan Road, Shanghai 200240, China*
[2]*Berkeley Center for Cosmological Physics and Department of Physics, University of California, Berkeley, California 94720, USA*
[3]*Lawrence Berkeley National Laboratory, 1 Cyclotron Road, Berkeley, California 94720, USA*

(Received January 1, 2018; Revised January 7, 2018; Accepted May 23, 2022)

Submitted to ApJ

## ABSTRACT

We propose a new velocity reconstruction method based on the displacement estimation by recently developed methods. The velocity is first reconstructed by transfer functions in Lagrangian space and then mapped into Eulerian space. High resolution simulations are used to test the performance. We find that the new reconstruction method outperforms the standard velocity reconstruction in the sense of better cross-correlation coefficient, less velocity misalignment and smaller amplitude difference. We conclude that this new method has the potential to improve the large-scale structure sciences involving a velocity reconstruction, such as kinetic Sunyaev-Zel'dovich measurement and supernova cosmology.

*Keywords:* cosmology: large-scale structure of universe

## 1. INTRODUCTION

Reconstructing the velocity field from density is a non-trivial procedure due to the high nonlinearity in the evolved density field and the non-local relationship with the velocity field. Also, usually we only have discrete and biased tracers such as galaxies in the observation, which suffer from density bias, shot noise and stochasticity. Early attempts, e.g. Nusser & Davis (1994), Fisher et al. (1995), and etc, aim to estimate the peculiar velocities from the early pioneer galaxy surveys. These results improved our knowledge of the Local Universe.

The accelerating expansion of our Universe concluded from the supernova observation is a great success in modern cosmology. It utilizes the luminosity distance and redshift relation to constrain the cosmological models. The Doppler effect by the peculiar velocity is one of the systematics in the supernova cosmology. Neglecting correlated peculiar velocities can cause an error in the best-fit value of the dark energy equation-of-state and also an overestimate of the precision of the measurement (Cooray & Caldwell (2006); Hui & Greene (2006); Davis et al. (2011)). The low-redshift cutoff is usually applied in order to avoid this systematics. For future Supernova surveys achieving statistical error bars less than about 2%, it is important to correct the peculiar velocity.

The kinetic Sunyaev-Zel'dovich (kSZ) effect offers a unique opportunity to characterize the cosmic peculiar velocity field in the distant Universe, and to search for the missing baryons. The kSZ measurement benefits from the velocity estimates for avoiding the cancellation of equally likely positive and negative kSZ signals (DeDeo et al. (2005); Ho et al. (2009); Shao et al. (2011); Li et al. (2014); Smith et al. (2018)). The significance level depends on the velocity estimation/reconstruction performance. In recent years, there have been a series of works to detect and measure the kSZ signal. Hand et al. (2012) first reported the detection of the kSZ signal by applying the pairwise kSZ estimator to ACT cosmic microwave background (CMB) data using a galaxy catalog from the SDSS III DR9. This measurement was achieved with higher precision using the BOSS DR11 catalogue (De Bernardis et al. (2017)). With the Planck CMB map, Planck Collaboration et al. (2016) reported a kSZ detection using the Central Galaxy Catalogue extracted from SDSS DR7 and Li et al. (2018) presented the measurement using BOSS data. Most of the velocity reconstruction methods used in the above literature are motivated by the linearized continuity equation. One can solve for the velocity field from the observed density field with some pre-processing such as de-biasing, smoothing, redshift-space distortion (RSD) correction and Gaussianization. The reconstruction is performed in Eulerian space and only the irrotational part is reconstructed by design. For future CMB-S4 surveys and Stage-IV galaxy surveys, remote dipole and quadrupole reconstruction

from the kSZ effect will benefit from a precisely reconstructed velocity field (Cayuso et al. (2018); Deutsch et al. (2018); Pan & Johnson (2019); McCarthy & Johnson (2019)).

Some physical quantities in Lagrangian space suffer less nonlinear effects and they provide us alternative angles to study the behavior of our Universe. Compared to the density field, the velocity field suffers from less nonlinear effects. The displacement field is an integral of the velocity field over cosmic time. Thus, these two fields are expected to have good correlation due to the low nonlinearity. By investigation of the relation between the displacement and the velocity in Lagrangian space, one can develop new velocity reconstruction methods. It is worth exploration to reconstruct the velocity in Lagrangian space given that the displacement can be well estimated from the nonlinear density field by recently developed algorithms.

These algorithms were proposed to reconstruct the initial condition from the nonlinear density map, which improves the signal-to-noise in the measurement of the baryon acoustic oscillation sound horizon scale (Zhu et al. (2017); Schmittfull et al. (2017); Shi et al. (2018); Hada & Eisenstein (2018)). The performance on the biased tracers such as the simulated halos/HOD galaxy samples are tested in Yu et al. (2017); Birkin et al. (2019); Hada & Eisenstein (2019). Despite the different theoretical motivation and operational procedure in the above backward modeling studies, the key to the improvement is same, a better estimate of the nonlinear displacement. Note that the initial condition/displacement could also be obtained from the forward modeling methods such as Hamiltonian Markov Chain Monte Carlo method (Wang et al. (2014)), optimization with Bayesian approach Seljak et al. (2017); Modi et al. (2018); Schmidt et al. (2019)), and etc.

It is worth notice that the reconstruction of the displacement also inspires many potential applications. The reconstructed displacement is an effective displacement which ensures the correct clustering but ignores some complicated process like shell-crossing. Understanding the reconstructed displacement may help us develop fast mock generation method. Given the nonlinear density field with RSD effect, the reconstructed one also contains RSD information and this may improve the RSD modelling since the RSD is more linear post to the reconstruction (Zhu et al. (2018)). The reconstructed displacement is also useful to measure the relative velocity of the neutrino to DM, which contains important information on the neutrino mass (Zhu & Castorina (2019)). The reconstructed displacement also helps in moving the observable in Eulerian space back to its Lagrangian position where it is more physically originated (such as the angular momentum of the galaxy, Yu et al. (2019)).

This paper presents our investigation on the velocity reconstruction based on the recently proposed displacement reconstruction methods. In Section 2, theoretical bases of the standard velocity reconstruction method and the new proposed velocity reconstruction are introduced and the algorithm is presented. In Section 4, we present the performance of the new velocity reconstruction. Section 6 summarizes the results and discuss. The extra layer of complication in observation, such as the shot noise and stochasticity for biased tracers, survey mask and RSD effect, is out of the scope of this paper and will be addressed in future investigation.

## 2. MOTIVATION

### 2.1. *Standard reconstruction*

Standard velocity reconstruction method adopts the linearized continuity equation,

$$\frac{\partial \delta(\boldsymbol{x})}{\partial t} + \nabla \cdot \boldsymbol{v}(\boldsymbol{x}) = 0 \ , \tag{1}$$

to convert the density maps into velocity maps. The reconstructed velocity field is obtained by the relation in Fourier space.

$$\boldsymbol{v}_r(\boldsymbol{k}) = afH \frac{i\boldsymbol{k}}{k^2} \frac{\delta_S(\boldsymbol{k})}{b} \ , \tag{2}$$

in which Gaussian smoothing is usually adopted to reduce the impact from the highly non-Gaussian region and meanwhile linearize the field, and galaxy bias is corrected. The prefactor $afH$ comes from the linear theory. $H$ is the Hubble parameter, $f = d\ln D/d\ln a$, and $D$ is the linear growth rate. Throughout the paper, we denote the reconstructed velocity with a subscript $r$ and the true velocity field is labelled with a subscript $t$.

For the purpose of velocity reconstruction, widely adopted Gaussian smoothing might not be optimal. There exist other schemes trying to achieve better performance. For example, one can linearize the density field by a logarithmic transform, and/or obtaining the velocity field using second order Lagrangian perturbation theory (See Planck Collaboration et al. (2016) for detailed velocity reconstruction comparison for the purpose of kSZ measurement).

Here we extend the standard reconstruction formalism to use the transfer function to ensure that the process is under an optimal manner,

$$\boldsymbol{v}_r(\boldsymbol{k}) = \frac{i\boldsymbol{k}}{k^2} T(k) \delta(\boldsymbol{k}) \ . \tag{3}$$

The transfer function is defined to minimize the error in the reconstruction, and is calibrated from the simulation.

### 2.2. *Reconstruction in Lagrangian space*

In the Lagrangian scenario, the motion of the fluid element is labeled by its original position $\boldsymbol{q}$ and specified by the displacement $\boldsymbol{\Psi}(\boldsymbol{q},t)=\boldsymbol{x}(t)-\boldsymbol{q}$ at time $t$. The Lagrangian perturbation theory attempts to model the nonlinear displacement in a perturbative way,

$$\boldsymbol{\Psi}=\boldsymbol{\Psi}^{(1)}+\boldsymbol{\Psi}^{(2)}+\cdots\ , \tag{4}$$

in which each term collects the contribution from the same order,

$$\begin{aligned}\boldsymbol{\Psi}^{(n)}(\boldsymbol{k})=&\frac{iD^n}{n!}\int\frac{d^3k_1}{(2\pi)^3}\cdots\frac{d^3k_n}{(2\pi)^3}(2\pi)^3\delta^D\left(\sum_{j=1}^{n}\boldsymbol{k}_j-\boldsymbol{k}\right)\\&\times\boldsymbol{L}^{(n)}\left(\boldsymbol{k}_1,\ldots,\boldsymbol{k}_n\right)\delta_L\left(\boldsymbol{k}_1\right)\cdots\delta_L\left(\boldsymbol{k}_n\right)\ ,\end{aligned} \tag{5}$$

with $\boldsymbol{k}=\boldsymbol{k}_1+\cdots+\boldsymbol{k}_n$. The first and second order kernels are given by

$$\boldsymbol{L}^{(1)}\left(\boldsymbol{k}_1\right)=\frac{\boldsymbol{k}}{k_1}\ , \tag{6}$$

$$\boldsymbol{L}^{(2)}\left(\boldsymbol{k}_1,\boldsymbol{k}_2\right)=\frac{3}{7}\frac{\boldsymbol{k}}{k^2}\left[1-\left(\frac{\boldsymbol{k}_1\cdot\boldsymbol{k}_2}{k_1k_2}\right)^2\right]\ . \tag{7}$$

The displacement divergence $\delta_\psi=-\nabla\cdot\boldsymbol{\Psi}$ is given by

$$\delta_\psi(\boldsymbol{k})=\delta^{(1)}(\boldsymbol{k})+\delta^{(2)}(\boldsymbol{k})+\cdots\ , \tag{8}$$

where the first order is just the linear density field, $\delta^{(1)}(\boldsymbol{k})=\delta_L(\boldsymbol{k})$, and

$$\begin{aligned}\delta^{(2)}(\boldsymbol{k})=&\frac{1}{7}\int\frac{d^3k_1}{(2\pi)^3}\frac{d^3k_2}{(2\pi)^3}(2\pi)^3\delta^D\left(\boldsymbol{k}_1+\boldsymbol{k}_2-\boldsymbol{k}\right)\\&\times\left\{1-\frac{3}{2}\left[\left(\frac{\boldsymbol{k}_1\cdot\boldsymbol{k}_2}{k_1k_2}\right)^2-\frac{1}{3}\right]\right\}\delta_L(\boldsymbol{k}_1)\delta_L\boldsymbol{k}_2)\ ,\end{aligned} \tag{9}$$

or equivalently in configuration space,

$$\delta^{(2)}(\boldsymbol{q})=\frac{1}{7}\delta_L^2(\boldsymbol{q})-\frac{1}{7}K^2(\boldsymbol{q})\ . \tag{10}$$

The tidal term $K^2(\boldsymbol{q})$ is give by the contraction of the tidal tensor,

$$K^2(\boldsymbol{q})=\frac{3}{2}K_{ij}(\boldsymbol{q})K_{ij}(\boldsymbol{q})\ , \tag{11}$$

where

$$K_{ij}(\boldsymbol{k})=\left(\frac{k_ik_j}{k^2}-\frac{1}{3}\delta_{ij}\right)\delta_L(\boldsymbol{k})\ . \tag{12}$$

Note that both $\boldsymbol{\Psi}(\boldsymbol{q})$ and $\delta_\psi(\boldsymbol{q})$ are in Lagrangian configuration space.

The velocity is the time derivative of the displacement. Thus, the Lagrangian velocity is the summation of the contributions from all orders,

$$\boldsymbol{v}(\boldsymbol{q})=a\dot{\boldsymbol{\Psi}}(\boldsymbol{q})=afH\boldsymbol{\Psi}^{(1)}+2afH\boldsymbol{\Psi}^{(2)}+\cdots\ , \tag{13}$$

in which the prefactors in each term come from the linear theory for $\boldsymbol{v}$ and $\boldsymbol{\Psi}$. In general case, the velocity divergence is related to densities by a series of transfer functions at each order,

$$\theta(\boldsymbol{k})=T_1(k)\delta_L(\boldsymbol{k})+T_2(k)\delta^{(2)}(\boldsymbol{k})+\cdots\ . \tag{14}$$

Once the linear density field is estimated, one can convert it to the Lagrangian velocity field and further map it into Eulerian space.

## 3. IMPLEMENTATION

### 3.1. *Simulation setup*

To test and compare the velocity reconstruction methods, we use a high resolution simulation involving $2048^3$ dark matter particles in a box with a side length of 600 $h^{-1}$Mpc. It is run by the particle-particle-particle-mesh N-body simulation code `CUBEP`$^3$`M` (see Harnois-Déraps et al. (2013)). The cosmic velocity field has a large correlation scale, typically $\sim 150h^{-1}$Mpc. This simulation box size is insufficient for robust large scale velocity statistics measurement. However, the following results are mainly based on the cross-correlation analysis. Due to the cancellation of the sample variance, it is sufficient to obtain reliable results. The reconstruction and analysis is performed on $512^3$ grids. We assign particle velocity onto uniform grids by the nearest particle (NP) method. Sampling artifacts in the E-mode power spectrum measurement associated with the NP assignment could be neglected in this configuration since the number density of $\sim 1(h^{-1}\mathrm{Mpc})^{-3}$ is sufficiently high (see Zhang et al. (2015); Zheng et al. (2015)).

### 3.2. *Reconstruction algorithm*

We use three recently developed nonlinear reconstruction algorithms in this work. They are described in Zhu et al. (2017), Shi et al. (2016) and Schmittfull et al. (2017). We denote them as A1, A2 and A3, respectively. They all provide the reconstructed density field which has significantly improved correlation with the linear initial condition. Although the performance in recovering the cross-correlation coefficient is similar, these three independently developed procedures produce different behaviors in the reconstructed density field. This leads to slightly different performance for the velocity

reconstruction. In the main result below we only show the result from A2 and present the difference in the Appendix.

Once we obtain the reconstructed density field, based on Eq. 14, we propose the direct velocity reconstruction in Lagrangian space by only using the first order term ($\mathcal{O}(1)$ reconstruction),

$$\theta_r(\boldsymbol{k}) = T_1(k)\delta_r(\boldsymbol{k}) \ . \tag{15}$$

Here $\delta_r$ is the reconstructed linear density field and the transfer function is defined as

$$T_1(k) = \frac{\langle \delta_r \theta_t \rangle}{\langle \delta_r \delta_r \rangle} \ . \tag{16}$$

It is calibrated by the reconstructed density $\delta_r(\boldsymbol{q})$ and the true Lagrangian velocity divergence $\theta_t(\boldsymbol{q})$ in simulation.

The reconstructed displacement contains nonlinear information. The high order terms may contain useful information to reconstruct the nonlinear velocity field. Similar to Schmittfull et al. (2017), we propose the $\mathcal{O}(2)$ reconstruction by further taking the second term in Eq. 14 into consideration.

First, for the estimated linear density field $\delta_r$, we use Wiener filter to remove the spurious power induced by the reconstruction algorithm,

$$\begin{aligned} W_{\rm WF}(k) &= \frac{\langle \delta_L \delta_r \rangle}{\langle \delta_r \delta_r \rangle} \ , \\ \delta_r^{(1)}(\boldsymbol{k}) &= \delta_r(\boldsymbol{k}) W_{\rm WF}(k) \ . \end{aligned} \tag{17}$$

Note that the reconstructed density field from different algorithms have different noise power, and thus different Wiener filter.

The second order term $\delta_r^{(2)}$ is calculated as Eq. 10 by replacing $\delta_L$ with $\delta_r^{(1)}$. However, due to the residual non-Gaussianity in $\delta_r^{(1)}$, $\langle \delta_r^{(1)} \delta_r^{(2)} \rangle$ is non-zero. Thus, we can not directly perform second order reconstruction based on $\delta_r^{(2)}$, otherwise the reconstructed $\theta_r^{(1)}$ and $\theta_r^{(2)}$ are not independent. We use orthogonization technique (Schmittfull et al. (2018)) to remove the correlated part in $\delta_r^{(2)}$ and construct $\hat{\delta}_r^{(2)}$ which has no correlation with $\delta_r^{(1)}$,

$$\begin{aligned} W_\perp(k) &= \frac{\langle \delta_r^{(2)} \delta_r^{(1)} \rangle}{\langle \delta_r^{(1)} \delta_r^{(1)} \rangle} \ , \\ \hat{\delta}_r^{(2)}(\boldsymbol{k}) &= \delta_r^{(2)}(\boldsymbol{k}) - \delta_r^{(1)}(\boldsymbol{k}) W_\perp(k) \ . \end{aligned} \tag{18}$$

Then we can perform the first and second order velocity reconstruction in sequence. For the first order term,

$$\begin{aligned} T_1(k) &= \frac{\langle \delta_r^{(1)} \theta_t \rangle}{\langle \delta_r^{(1)} \delta_r^{(1)} \rangle} \\ \theta_r^{(1)}(\boldsymbol{k}) &= T_1(k) \delta_r^{(1)}(\boldsymbol{k}) \ . \end{aligned} \tag{19}$$

The residual is

$$\theta_m(\boldsymbol{k}) = \theta_t(\boldsymbol{k}) - \theta_r^{(1)}(\boldsymbol{k}) \ , \tag{20}$$

which ensures $\langle \theta_m \theta_r^{(1)} \rangle = 0$. For the second order term,

$$\begin{aligned} T_2(k) &= \frac{\langle \hat{\delta}_r^{(2)} \theta_m \rangle}{\langle \hat{\delta}_r^{(2)} \hat{\delta}_r^{(2)} \rangle} \ , \\ \theta_r^{(2)}(\boldsymbol{k}) &= T_2(k) \hat{\delta}_r^{(2)}(\boldsymbol{k}) \ . \end{aligned} \tag{21}$$

The $\mathcal{O}(2)$ reconstruction is $\theta_r = \theta_r^{(1)} + \theta_r^{(2)}$.

## 4. PERFORMANCE

### 4.1. *Lagrangian velocity*

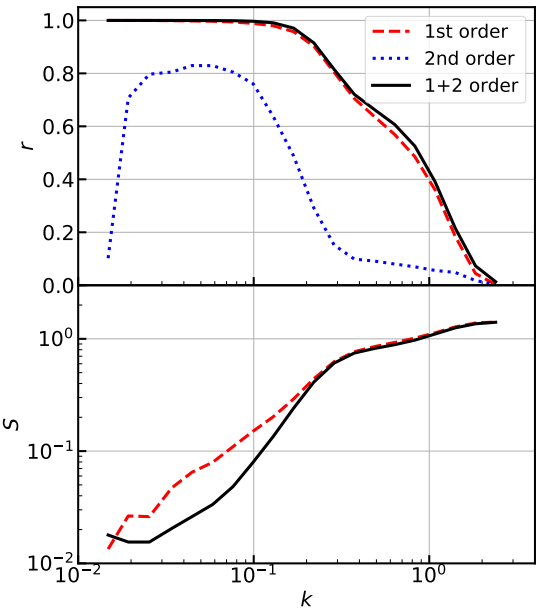


**Figure 1.** The upper panel shows the cross-correlation coefficient between $\delta_r^{(1)}$ and $\theta_t$, $\delta_r^{(2)}$ and $\theta_m$, and $\delta_r = \delta_r^{(1)} + \delta_r^{(2)}$ and $\theta_t$. They are presented in red dashed, blue dotted and black solid lines, respectively. The good cross-correlation is the base for the velocity reconstruction in Lagrangian space. The lower panel shows the stochasticity of the reconstructed velocity field relative to the true one in Lagrangian space. It is defined as $S = \sqrt{2(1-r)}$ and amplifies the difference at large scales where $r$ is very close to unity.

We first look at the reconstruction performance in Lagrangian space. The red dashed line in the upper panel of Fig. 1 shows the cross-correlation coefficient between the reconstructed density field $\delta_r^{(1)}(\boldsymbol{q})$ and the true velocity divergence in Lagrangian space $\theta_t(\boldsymbol{q})$. We found that at large scale of $k < 0.2\ h\mathrm{Mpc}^{-1}$ the cross-correlation is close to one, and towards small scale the coefficient decreases. At large scales, both the velocity and the displacement is linear. This naturally leads to

the almost perfect correlation at large scales. At small scales, both the velocity and the displacement suffer from the nonlinear effects. We expect the influence is more severe in the velocity field. These nonlinear effects change the small scale velocity substantially and cause the loss of the correlation with the displacement.

We also plot the cross-correlation between the second order term $\delta_r^{(2)}(\boldsymbol{q})$ and the residual velocity divergence $\theta_m(\boldsymbol{q}) = \theta_t(\boldsymbol{q}) - \theta_r^{(1)}(\boldsymbol{q})$ in blue dotted line. We also find a significant correlation, $r \sim 0.8$ at $0.02\ h\mathrm{Mpc}^{-1} < k < 0.2\ h\mathrm{Mpc}^{-1}$, implying that $\mathcal{O}(2)$ reconstruction could help. However, the amount of the improvement by adding this second order term also depends on the power relative to the first order term. The result for the $\mathcal{O}(2)$ reconstruction is shown in black solid line. Slightly improvement is seen at $k < 0.15\ h\mathrm{Mpc}^{-1}$ and $k > 0.4\ h\mathrm{Mpc}^{-1}$.

In the bottom panel we plot the stochasticity defined as $S = \sqrt{2(1-r)}$. This statistics amplifies the difference when $r \sim 1$. The $\mathcal{O}(1)$ reconstruction result is plotted in red dashed line and the $\mathcal{O}(2)$ reconstruction is in black solid line. From this panel we see that $\mathcal{O}(2)$ reconstruction has a lower stochasticity than the standard method by a factor of $\sim 3$ at $0.02\ h\mathrm{Mpc}^{-1} < k < 0.1\ h\mathrm{Mpc}^{-1}$. This suppression of the stochasticity at large scales is important for measuring the large scale effects such as the primordial non-Gaussianity by the sample variance cancellation technique (Münchmeyer et al. (2018)).

### 4.2. *Eulerian velocity*

After mapping the reconstructed Lagrangian velocity to Eulerian space by the displacement, we use the NP velocity assignment scheme to obtain the reconstructed velocity field. Note that the true velocity field is obtained by the same NP assignment. The cross-correlation coefficient between the two are presented in Fig. 2. The red dashed line, black solid line and blue dotted line represents the result for $\mathcal{O}(1)$ reconstruction, $\mathcal{O}(2)$ reconstruction and the standard reconstruction, respectively. We find that the proposed $\mathcal{O}(1)$ reconstruction method performs better than the standard one at scales $k > 0.1\ h\mathrm{Mpc}^{-1}$, and the $\mathcal{O}(2)$ reconstruction further slightly improves the cross-correlation coefficient at $0.1\ h\mathrm{Mpc}^{-1} < k < 1\ h\mathrm{Mpc}^{-1}$.

In the bottom panel of Fig. 2 we show the stochasticity for the above reconstruction methods. Adding $\mathcal{O}(2)$ reconstruction suppresses the stochasticity at scales $k < 1\ h\mathrm{Mpc}^{-1}$ relative to the $\mathcal{O}(1)$ reconstruction, and it performs better than the standard reconstruction method at scales $0.02\ h\mathrm{Mpc}^{-1} < k < 1\ h\mathrm{Mpc}^{-1}$.

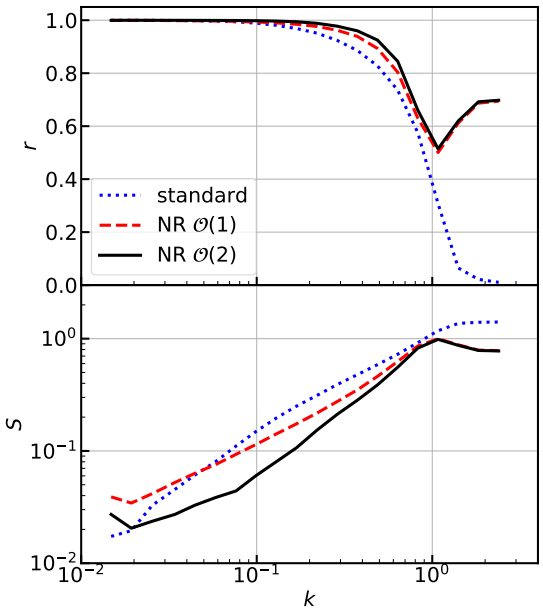


**Figure 2.** The upper panel shows the cross-correlation coefficient between the true Eulerian velocity field and the reconstructed velocity field by the standard reconstruction (blue dotted line), $\mathcal{O}(1)$ reconstruction (red dashed line) and $\mathcal{O}(2)$ reconstruction (black solid line). The lower panel shows the stochasticity induced by the reconstruction methods.

One obvious feature is that the cross-correlation coefficient decreases towards small scale for $k < 1\ h\mathrm{Mpc}^{-1}$ but increases at $k > 1\ h\mathrm{Mpc}^{-1}$. However, the result at $k > 1\ h\mathrm{Mpc}^{-1}$ is suspicious due to the fact that this scale is close to the Nyquist frequency of the analysis and this good correlation between the reconstructed and the true velocity may partially comes from the same systematics by the same velocity assignment.

We compare the reconstructed velocity with the true one at point-to-point level in Fig. 3, which shows the two dimensional histogram with the horizontal axis being the reconstructed velocity while the vertical axis being the true velocity. The color indicates the relative counts normalized to unity. The upper panel shows the result from $\mathcal{O}(2)$ reconstruction and the lower from the standard method. Compared to the standard reconstruction, we observe obvious slimmer contour for the $\mathcal{O}(2)$ reconstruction.

To quantify the performance, we check the direction and the amplitude of the reconstructed velocity. We define the cosine angle between it and the true one as

$$\mu = \frac{\boldsymbol{v}_t \cdot \boldsymbol{v}_r}{|\boldsymbol{v}_t||\boldsymbol{v}_r|} \ . \tag{22}$$

We plot this cosine angle for the new reconstruction and the standard one of one slice in the middle and bottom panel of Fig. 4, respectively. Also plotted is a dark

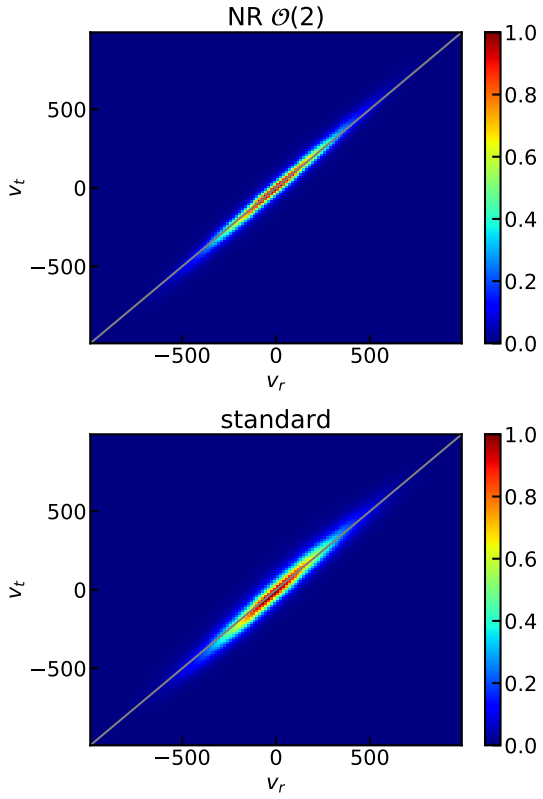


**Figure 3.** The upper panel shows the 2D histogram for the true velocity and the reconstructed velocity by the $\mathcal{O}(2)$ reconstruction. The lower panel is for the true velocity and the velocity reconstructed by the standard method. The new reconstruction results in tighter relation between the reconstructed velocity and the true one.

matter density of the same slice in the top panel. An obvious fact is that both reconstruction methods perform worse in the high density region, i.e. the highly nonlinear region. We find that for the $\mathcal{O}(2)$ reconstruction, the region with $\mu < 0.95$ (green to blue color) occupies far less volume than the standard reconstruction result, indicating that the new reconstruction performs well down to the nonlinear region.

The mean of the $\mu$ for the new reconstruction is 0.977, while the standard method has the mean $\langle\mu\rangle = 0.958$. This corresponds to the mean misalignment angle of 12.31 deg and 16.66 deg for the new reconstruction and the standard one, respectively. We also plot the histogram for the cosine angle $\mu$ in Fig. 5. The new reconstruction (blue histogram) has much more pixels with very good direction reconstruction ($\mu > 0.995$) than the standard method (red histogram).

We also check whether the amplitude of the velocity is reconstructed well. Here we define three kinds of velocity amplitude difference. The first one is the difference between the true velocity amplitude and the

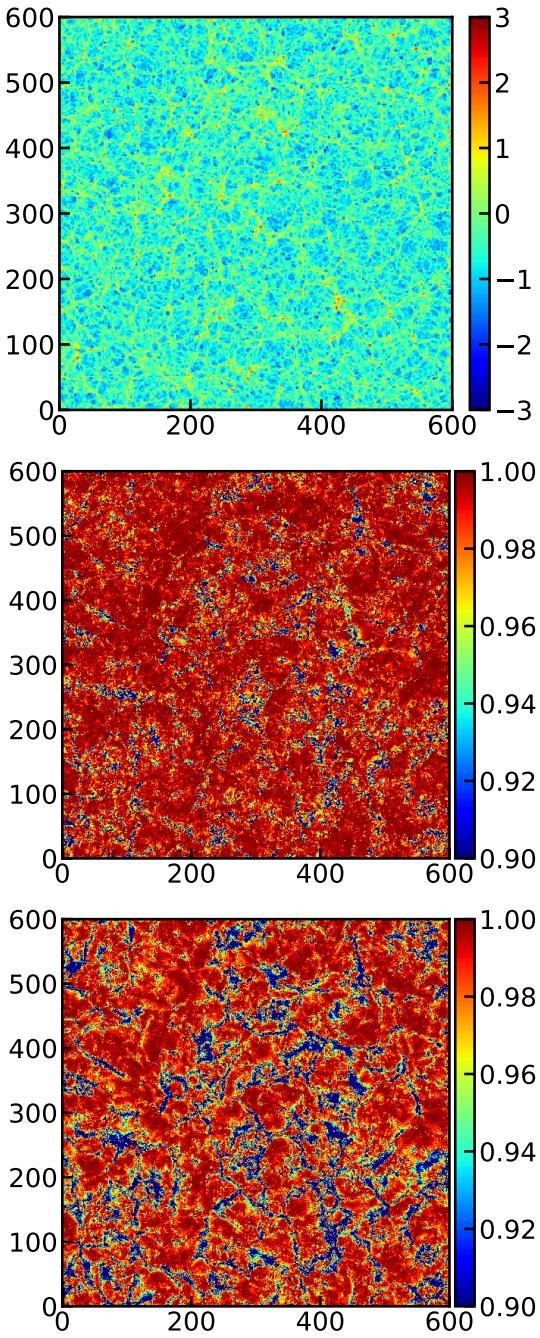


**Figure 4.** Top: a slice of DM density field $\log(1+\delta)$. Middle: a slice of the cosine angle between $v_t$ and $v_r$ reconstructed by the $\mathcal{O}(2)$ reconstruction. Bottom: a slice of the cosine angle between $v_t$ and $v_r$ reconstructed by the standard method. Large misalignment appears at high density region.

reconstructed one. The second is the difference between the true velocity and the projection of the reconstructed velocity on the true one, i.e. $\boldsymbol{v}_p = \boldsymbol{v}_r \cdot \boldsymbol{v}_t/|v_t|$. The last one is the difference between the velocity component in $z$-direction.

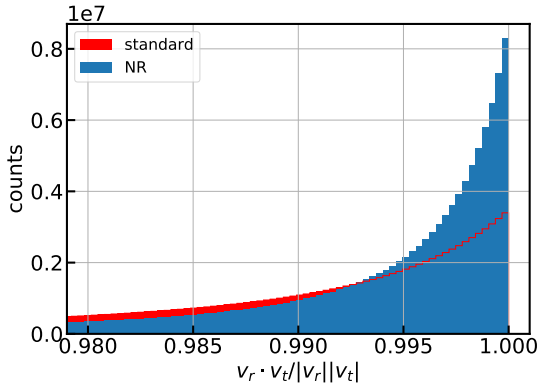


**Figure 5.** Distribution of the cosine angle between $\boldsymbol{v}_t$ and $\boldsymbol{v}_r$. The red histogram is for standard reconstruction, while the blue is for the new one. The $\mathcal{O}(2)$ reconstruction has much more pixels with $\mu > 0.993$. The average cosine angle is 0.9577 for standard reconstruction, corresponding to misalignment of 16.72 deg. For nonlinear reconstruction it is 0.9790 and 11.77 deg.

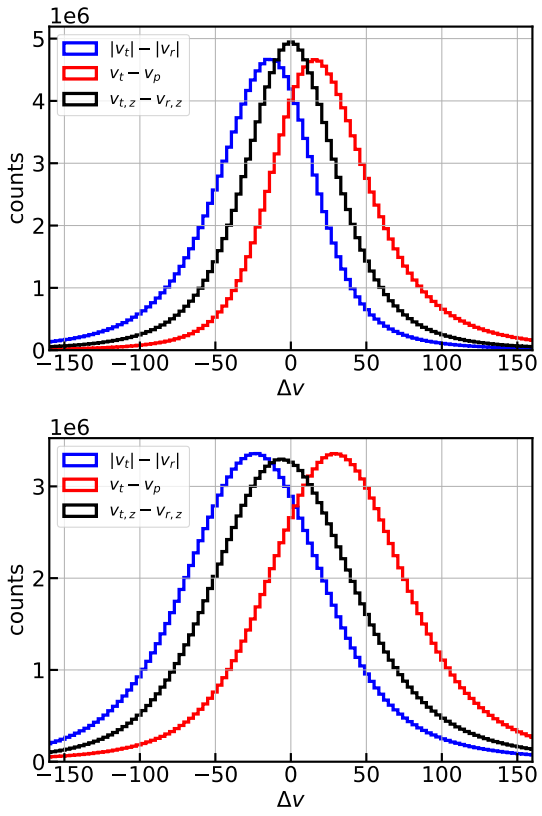


**Figure 6.** Blue: the magnitude difference between $\boldsymbol{v}_t$ and $\boldsymbol{v}_r$. Red: the difference between $\boldsymbol{v}_t$ and $\boldsymbol{v}_r$ projected on $\boldsymbol{v}_t$. Black: the difference between $\boldsymbol{v}_t$ and $\boldsymbol{v}_r$ in $z$-direction. Top panel is the result of the new reconstruction method, and bottom panel is of the standard reconstruction. The new reconstruction result presents smaller amplitude bias and smaller scatter in the distribution.

The results are shown in Fig. 6, in which the distribution of the velocity amplitude difference is plotted. The top plot is the result from the new reconstruction, while the bottom plot from the standard one. For the first and second distribution (blue and red histogram), the new reconstruction result has a peak closer to zero than the standard reconstruction, i.e. a smaller reconstruction bias in the amplitude. Furthermore, the new reconstruction also has smaller scatters in these distributions than the standard one. For the last statistics, the velocity difference in one direction, the standard method is expected to produce a mean of zero by design. For the new reconstruction, we also find this statistics has a mean of zero, and the width of the distribution is much narrower than the standard one. All the above statistics show that the new reconstruction has better performance in recovering the velocity amplitude.

## 5. RAMIFICATIONS

### 5.1. *Using simulated displacement*

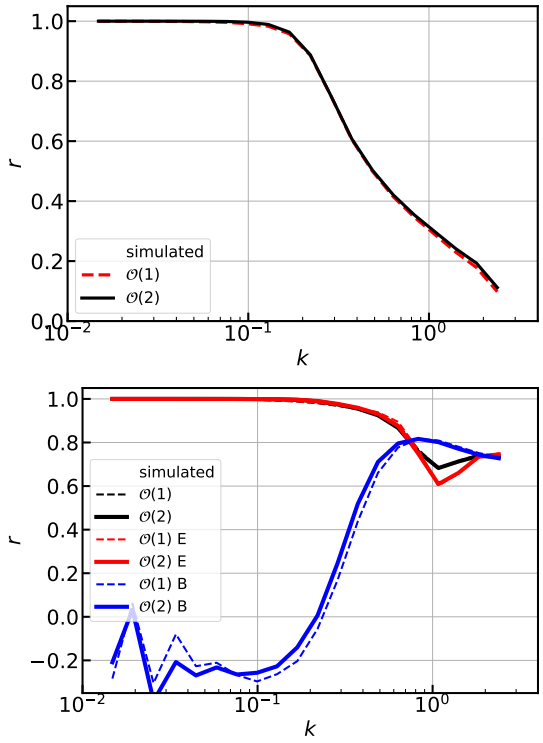


**Figure 7.** The result of the reconstruction using the simulated displacement. Top panel is the cross-correlation coefficient between $\boldsymbol{v}_r(\boldsymbol{q})$ and $\boldsymbol{v}_t(\boldsymbol{q})$ in Lagrangian space (red dashed line for $\mathcal{O}(1)$ and black solid line for $\mathcal{O}(2)$ reconstruction). Bottom panel is the cross correlation coefficient between $\boldsymbol{v}_r(\boldsymbol{x})$ and $\boldsymbol{v}_t(\boldsymbol{x})$ in Eulerian space. The total, E-mode and B-mode component result is presented in black, red and blue lines.

The above results slightly depend on the performance of the detailed reconstruction algorithm. We compare the performance of the three different algorithms in the Appendix. Here we want to know the up-limit of the velocity reconstruction in Lagrangian space. Thus, in this subsection we present the result under the assumption that the displacement estimation is perfect, i.e. the reconstruction is performed using the simulated displacement instead of the reconstructed one. The cross-correlation coefficient in Lagrangian space is shown in the top panel of Fig. 7. The red dashed line is the result from $\mathcal{O}(1)$ reconstruction and the black solid line is for $\mathcal{O}(2)$ reconstruction. In this case we see that the improvement by including second order term is very mild. The nonlinear displacement already includes almost all the information that can be used to reconstruct the nonlinear velocity field.

In the bottom panel we show the cross-correlation in Eulerian space. The performance is better than the results using reconstructed displacement. The cross-correlation coefficient between the reconstructed velocity and the true one reach 0.7 at $k \sim 1\ h\mathrm{Mpc}^{-1}$ (black solid line). No obvious difference between $\mathcal{O}(1)$ and $\mathcal{O}(2)$ reconstruction is observed and the black solid and black dashed line overlap with each other. We further decompose both the true and the reconstructed velocity field into curl-free E-mode and divergence-free B-mode and correlate them separately. The cross-correlation for the E-mode is slightly lower than the total velocity at scale $k \sim 1\ h\mathrm{Mpc}^{-1}$. The B-mode cross-correlation coefficient is $\sim -0.2$ at $k < 0.1\ h\mathrm{Mpc}^{-1}$ and rapidly increases to $\sim 0.8$ at $k \sim 0.7\ h\mathrm{Mpc}^{-1}$. Note that the observed B-mode suffers from severe systematics in this configuration (Refer to Fig. 12 in Zheng et al. (2013)) and the power spectrum changes significantly as the simulation configuration changes. We expect that the observed cross-correlation for the B-mode between the true velocity and the reconstructed one mainly comes from the systematics induced by the velocity assignment method, the finite volume effect and the aliasing effect.

### 5.2. *Considering B-mode in Lagrangian space*

In the above subsection, the reconstructed B-mode in Eulerian space comes from the nonlinear mapping and is converted from the E-mode in Lagrangian space. Due to the nonlinear evolution of the Universe, both the velocity and the displacement have B-mode component (see e.g. Chan (2014)) both in Eulerian and Lagrangian space. Here we are curious about whether the Lagrangian space B-mode correlation helps in the reconstruction. The cross-correlation between the two from simulation are shown in the red dashed line in the upper left panel of Fig. 8. Also plotted is the cross-correlation from the E-mode in black solid line. At large scales, the B-mode velocity and B-mode displacement also have a large cross-correlation coefficient $\sim 0.9$. It seems that this B-mode correlation could help in the velocity reconstruction. This also implies that the Cartesian components of the velocity and displacement field contains extra correlation other than the divergence of the two. In the upper right panel we show the cross-correlation coefficient between the true velocity and the velocity reconstructed 1) using the transfer function measured from the E-mode only ($\theta_r(\boldsymbol{k}) = T^E(k)\delta_r(\boldsymbol{k})$), 2) using the transfer function measured from the Cartesian components ($\boldsymbol{v}_{r,i}(\boldsymbol{k}) = T_i(k)\boldsymbol{\Psi}_{r,i}(\boldsymbol{k})$ and $i$ runs for 3 Cartesian components), and 3) using the transfer functions for E- and B-mode separately and summing the two reconstructed velocity fields ($\theta_r(\boldsymbol{k}) = T^E(k)\delta_r(\boldsymbol{k})$ and $\boldsymbol{v}^B_{r,i}(\boldsymbol{k}) = T^B(k)\boldsymbol{\Psi}^B_{r,i}(\boldsymbol{k})$).

We indeed see that adding the B-mode improves the velocity reconstruction in Lagrangian space. Reconstruction from the Cartesian components also improves the reconstruction but it performs worse than directly adding B-mode reconstruction since it neglects the correlation between different Cartesian components.

However, this improvement in Lagrangian space is mainly at scales $k > 0.2\ h\mathrm{Mpc}^{-1}$ and is not mapped into Eulerian space. In the bottom left panel of Fig. 8 we present the cross-correlation coefficient for the above three cases and for the total, E-mode and B-mode components separately. We find that including the B-mode information in Lagrangian space leads to worse performance in Eulerian space. We argue that the noise in the B-mode displacement (the part not correlated with the velocity) is converted into E-mode velocity in Eulerian, thus contaminating the velocity reconstruction instead of improving it. The bottom right panel shows the E- and B-mode power spectrum of the reconstructed velocity field and the true one. Including the B-mode correlation in Lagrangian space does not change the E-mode power spectrum in Eulerian space much, but the Eulerian B-mode power spectrum is changed significantly. This also implies that the B-mode is mainly a noise.

The A1 and A2 reconstruction algorithm has no B-mode displacement by design, but the A3 has. In the left panel of Fig. 9, we find that this estimated B-mode displacement has a weaker correlation ($r \sim 0.5$) with the true B-mode velocity compared with the case using the real simulated displacement. Thus, it suffers from more severe noise than the previous case. It is expected that the reconstruction by adding the B-mode in Lagrangian space performs worse in Eulerian space. This is observed in the right panel of Fig. 9).

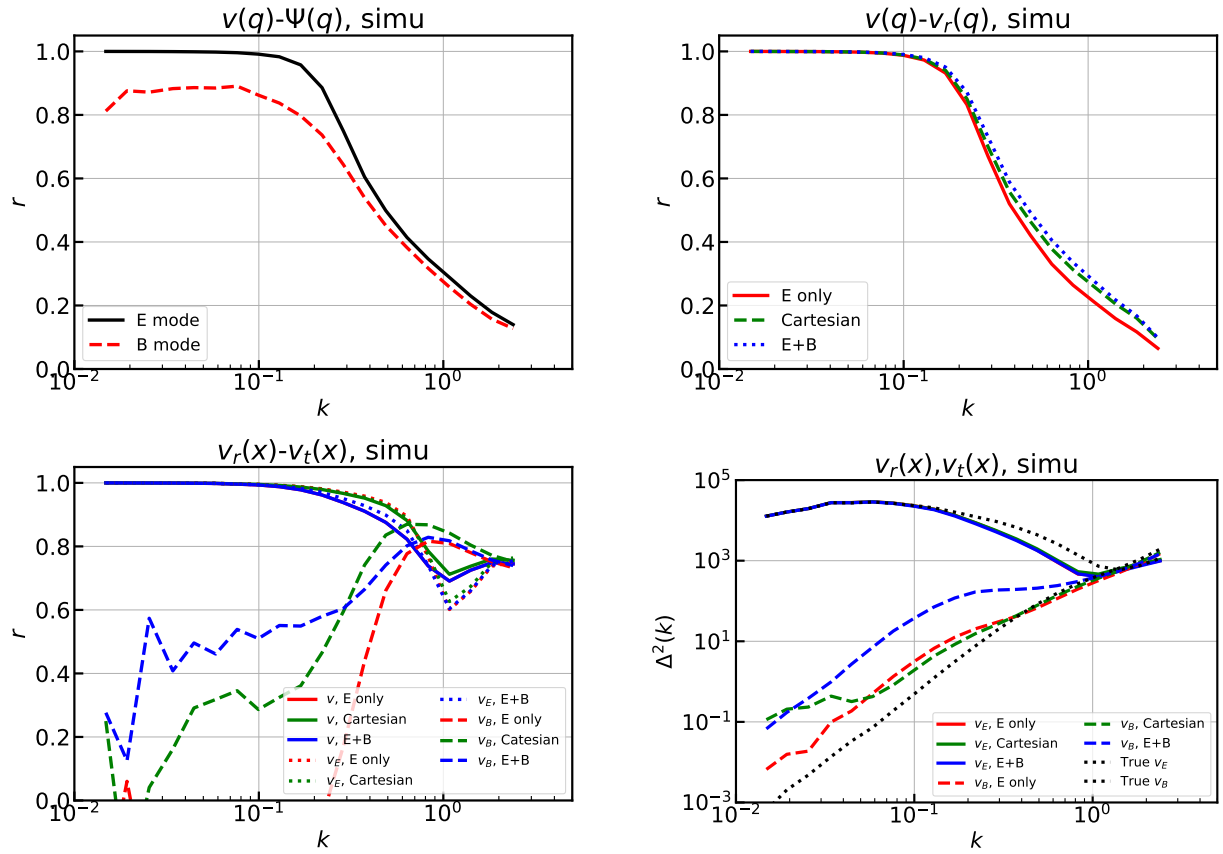


**Figure 8.** The upper left panel shows the cross-correlation coefficient between the Lagrangian velocity and displacement in simulation. The E-mode correlation is in black solid line and the result for B-mode component is in red dashed line. The upper right panel shows the the cross-correlation coefficients between the reconstructed velocity and the true one in Lagrangian space. Three cases correspond to E-mode only reconstruction, reconstruction for 3 Cartesian directions separately, and reconstruction for E- and B-mode separately. The bottom left panel is the cross-correlation between the reconstructed velocity and the true one in Eulerian space for different cases. The bottom right panel is the results for power spectrum comparison.

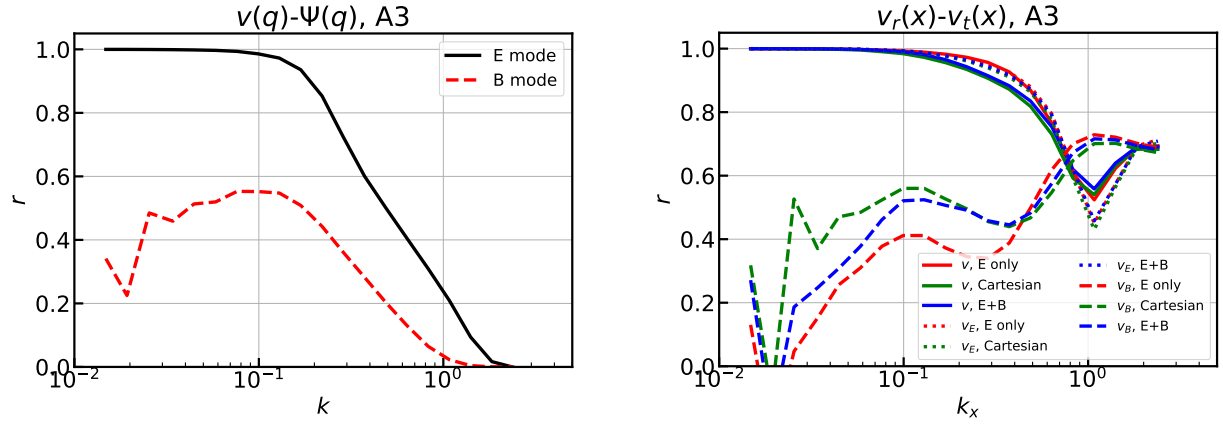


**Figure 9.** Same as the corresponding panels in Fig. 8, but for the reconstructed displacement by the A3 method.

### 5.3. *Using linear displacement*

For the purpose of mock construction, it is straightforward to start with a linear density field. Here we test the performance by velocity reconstruction from the linear density field. Combined with the fast density map generation methods such as 1LPT, 2LPT or other techniques, we may obtain mocks with both good density

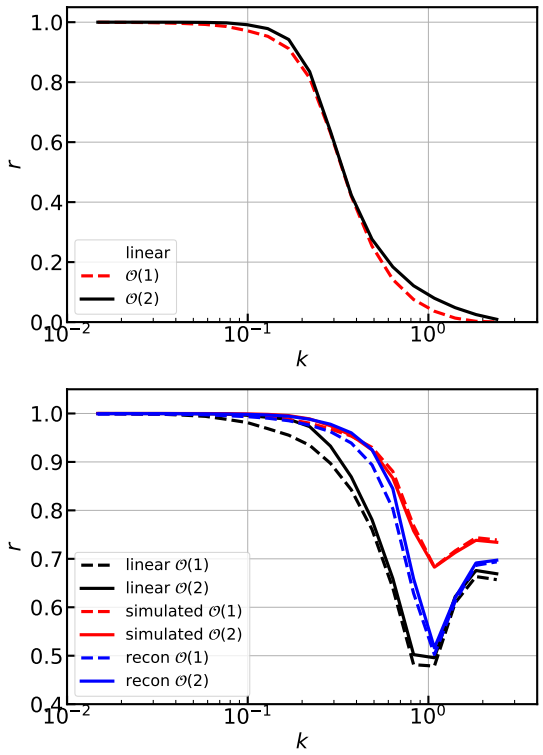


**Figure 10.** The $\mathcal{O}(1)$ and $\mathcal{O}(2)$ reconstruction using the linear density. Top panel is the cross-correlation in Lagrangian space. Bottom panel is the result in Eulerian space. Also plotted in the bottom panel is the cross-correlation result using the simulated and the reconstructed displacement for comparison.

and velocity field. These synthetic mocks are of great importance for future surveys.

The process is roughly same as the reconstruction with the simulated displacement. We just use the linear density field to replace the simulated displacement divergence in the reconstruction algorithm. Since the linear density is Gaussian, no orthogonization is needed.

The transfer function in this case is measured by

$$T_1(k) = \frac{\langle \delta_L \theta_t \rangle}{\langle \delta_L \delta_L \rangle} \ , \\ \theta_r^{(1)}(\boldsymbol{k}) = T_1(k)\delta_L(\boldsymbol{k}) \ . \tag{23}$$

We could also perform $\mathcal{O}(2)$ reconstruction by further measuring the second transfer function from the second order LPT density field $\delta^{(2)}$ and the residual velocity field $\theta_m = \theta_t - \theta_r^{(1)}$.

$$T_2(k) = \frac{\langle \delta^{(2)} \theta_m \rangle}{\langle \delta^{(2)} \delta^{(2)} \rangle} \ , \\ \theta_r^{(2)}(\boldsymbol{k}) = T_2(k)\delta^{(2)}(\boldsymbol{k}) \ . \tag{24}$$

In this case, the $\mathcal{O}(2)$ reconstruction (i.e., 2LPT) captures more nonlinear velocity information than $\mathcal{O}(1)$ reconstruction (i.e., 1LPT). This is observed in the top panel of Fig. 10. $\mathcal{O}(2)$ reconstruction increases the cross-correlation coefficient at $k \sim 0.1\ h\mathrm{Mpc}^{-1}$ and $k \sim 1\ h\mathrm{Mpc}^{-1}$ in Lagrangian space.

In the bottom panel, we compare the velocity cross-correlation coefficient in Eulerian space by the reconstruction using the linear displacement (black lines), using the simulated nonlinear displacement (red lines) and using the reconstructed displacement (blue lines). The $\mathcal{O}(1)$ reconstruction is presented in dashed line and $\mathcal{O}(2)$ in solid line. From this plot we clearly see that the case using the nonlinear or reconstructed displacement has better performance than the case using linear displacement. We also notice that the velocity reconstruction performance using the reconstructed displacement catches the up-limit down to scale $k \sim 0.7\ h\mathrm{Mpc}^{-1}$.

### 5.4. *Improvement by real space transfer functions*

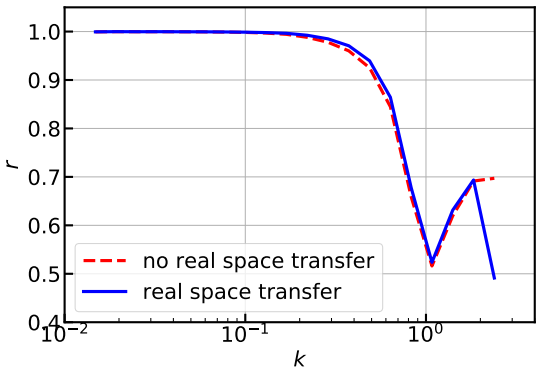


**Figure 11.** The red dashed line presents the cross-correlation coefficient between the reconstructed velocity and the true velocity field. The blue solid line is the result that two real space transfer functions are applied to make an optimal combination of the E- and B-mode component. A very mildly improvement is observed.

According to the result in Section 5.2, we should only use the E-mode displacement in the reconstruction and the reconstructed velocity field is irrotational in Lagrangian space by design. However, after mapping to Eulerian space, a part of the E-mode is converted into B-mode. To obtain a better velocity reconstruction in real space, we could measure two more transfer functions in Eulerian space to adjust the reconstructed E- and B-mode component.

$$T^E(k) = \frac{\langle v_r^E v_t^E \rangle}{\langle v_r^E v_r^E \rangle} \ , \\ T^B(k) = \frac{\langle v_r^B v_t^B \rangle}{\langle v_r^B v_r^B \rangle} \ , \tag{25}$$

and $\boldsymbol{v}_r(\boldsymbol{k}) = T^E(k)\boldsymbol{v}_r^E(\boldsymbol{k}) + T^B(k)\boldsymbol{v}_r^B(\boldsymbol{k})$. The result is presented in Fig. 11. A very mild improvement is observed in the cross-correlation coefficient at $k \sim 0.5\ h\mathrm{Mpc}^{-1}$. Considering that the improvement is negligible and this process may induce noise instead of improving the performance if the transfer function is not sufficiently accurate, we do not propose to apply this final step in the reconstruction.

## 6. CONCLUSION AND DISCUSSION

We propose a new velocity reconstruction method based on the estimated displacement field from the nonlinear density maps by recently developed algorithms. The reconstruction is first performed in Lagrangian space by the calibrated transfer functions, and then the Eulerian velocity is obtained by the mapping. We found that this new velocity reconstruction has better performance than the standard reconstruction method based on the linearized continuity equation. It produces a velocity field with better cross-correlation coefficient, less velocity misalignment and smaller amplitude difference with the true one. Generally, $\mathcal{O}(2)$ reconstruction outperforms $\mathcal{O}(1)$ reconstruction by taking use of the velocity information residing in the high order terms. A summary of the statistics we investigated is presented in Table 1.

We explored several extensions. One extension is to consider the correlation between the B-mode component of the velocity and displacement. The other one adopts two more transfer functions in real space to adjust the reconstructed E-mode the B-mode components in Eulerian space. However, the performance is not improved or very mild. Thus, it complicates the process and is not paid off.

We also explored the up-limit of this new reconstruction method by assuming the displacement is perfectly reconstructed. We found that in this case the difference between $\mathcal{O}(1)$ and $\mathcal{O}(2)$ is very small. One surprising point is that the $\mathcal{O}(2)$ reconstruction performance from A2 is very close to this up-limit in the sense of cross-correlation coefficient and the misalignment angle. We also attempted to obtain the velocity field from the linear displacement by the same approach. This presents the limit we can reach by only using the 1LPT and 2LPT displacement and the transfer functions with calibration.

The reconstruction performance from biased tracer depends on the understanding of the bias. Wang & Pen (2019) found that the acoustic peaks are recovered best when the linear bias is correctly removed, and thus it is possible to obtain an estimation of the bias in the process of the reconstruction. For the low density sample with only massive halos, correction of the bias is important. Otherwise the overestimation of the displacement amplitude significantly degrades the linear density reconstruction. For high density sample with bias less than unity, the bias does not influence the results much (e.g. Birkin et al. (2019)). We leave the quantification of the velocity reconstruction performance from the biased tracer into future investigation.

With the reconstructed initial condition of some volume of the Universe, one could perform the simulation to obtain the velocity field. However, the reconstruction induces noise and non-Gaussianity in the linear density field. The comparison between the constrained simulation and the original one has not been investigated for these reconstruction algorithms. We also leave the comparison of both the density and the velocity between the constraint simulation and the true one in the future.

## ACKNOWLEDGEMENT

We thank Baojiu Li for providing the reconstruction codes and Pengjie Zhang for useful discussions. This work was supported by the National Key Basic Research and Development Program of China (No. 2018YFA0404504), the National Science Foundation of China (grant No. 11773048, 11403071).

## APPENDIX

### A. COMPARISON OF A1, A2 AND A3

In this work we adopted the three algorithms A1, A2 and A3. They are described in Zhu et al. (2017); Schmittfull et al. (2017); Shi et al. (2018), respectively. These tests have not been performed in a systematical way before and a brief comparison is presented here. We use the default parameters proposed in these literature since the simulation and analysis configuration is similar. The result of the reconstructed Lagrangian velocity is presented in Fig. 12. The solid red, dashed green and dotted blue lines are for A1, A2 and A3, respectively. The left panel is the cross-correlation coefficient of the reconstructed and true velocity in Lagrangian space, while the right panel is for the Eulerian space. We find the A2 has the best cross-correlation coefficient in Lagrangian space. The good performance is also mapped into Eulerian space, leading to the best cross-correlation coefficient for Eulerian velocity. However, A1 has the similar

**Table 1.** A summary of the performance from different reconstruction methods, including the standard reconstruction, the $\mathcal{O}(1)$ and $\mathcal{O}(2)$ nonlinear reconstruction by three recently developped algorithms, the reconstruction using the simulated displacement and with the linear density field.

| | $\mu$ | $\Delta v$ mean | $\Delta v$ r.m.s | $v_t - v_p$ mean | $v_t - v_p$ r.m.s | $\Delta v_z$ mean | $\Delta v_z$ r.m.s |
|---|---|---|---|---|---|---|---|
| standard | 0.958 | 23.3 | 73.6 | 35.8 | 78.7 | 0.02 | 75.5 |
| A1 $\mathcal{O}(1)$ | 0.965 | -6.34 | 71.8 | 3.25 | 77.9 | -17.6 | 62.3 |
| A1 $\mathcal{O}(2)$ | 0.968 | 10.2 | 64.2 | 18.7 | 69.6 | -16.1 | 57.8 |
| A2 $\mathcal{O}(1)$ | 0.971 | 5.10 | 67.3 | 13.4 | 72.9 | 0.08 | 61.4 |
| A2 $\mathcal{O}(2)$ | 0.977 | 23.5 | 57.5 | 29.9 | 62.7 | 0.07 | 55.4 |
| A3 $\mathcal{O}(1)$ | 0.970 | 5.71 | 70.7 | 14.2 | 78.2 | 9.19 | 63.7 |
| A3 $\mathcal{O}(2)$ | 0.972 | 19.9 | 63.9 | 27.7 | 70.5 | 9.75 | 60.7 |
| simulated $\mathcal{O}(1)$ | 0.978 | 10.9 | 62.1 | 17.4 | 69.3 | 0.04 | 56.5 |
| simulated $\mathcal{O}(2)$ | 0.979 | 17.2 | 56.0 | 23.3 | 63.3 | 0.05 | 54.0 |
| linear $\mathcal{O}(1)$ | 0.955 | 6.25 | 88.8 | 18.9 | 95.9 | 0.02 | 77.9 |
| linear $\mathcal{O}(2)$ | 0.963 | 20.2 | 70.9 | 30.2 | 78.1 | 0.10 | 67.4 |

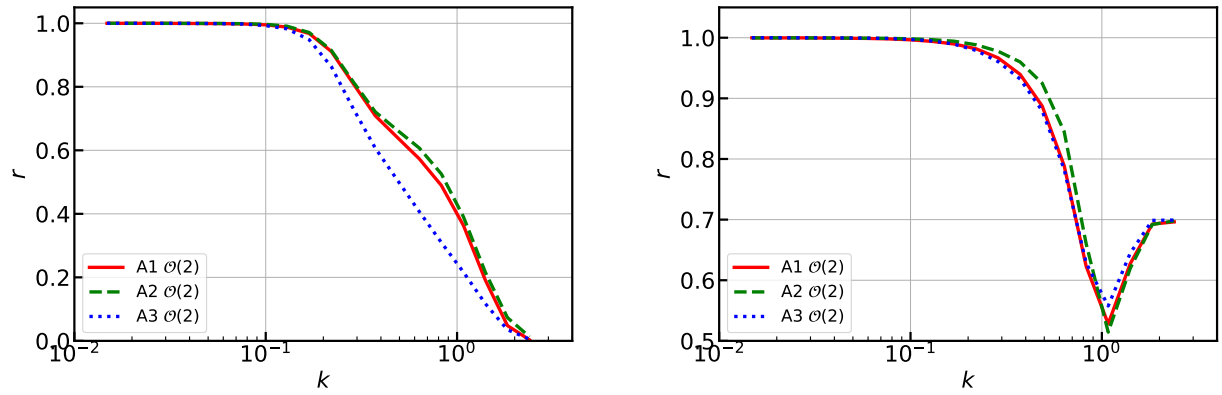


**Figure 12.** The comparison among the three recently developped reconstruction algorithms. The left panel shows the cross-correlation coefficients between the true velocity and the $\mathcal{O}(2)$ reconstructions in Lagrangian space and the right panel shows the coefficients in Eulerian space.s

but slightly worse performance than A2 in Lagrangian space, and has the similar performance with A3 in Eulerian space. A summary is presented in Table 1.

## REFERENCES


Birkin, J., Li, B., Cautun, M., & Shi, Y. 2019, MNRAS, 483, 5267

Cayuso, J. I., Johnson, M. C., & Mertens, J. B. 2018, PhRvD, 98, 063502

Chan, K. C. 2014, PhRvD, 89, 083515

Cooray, A., & Caldwell, R. R. 2006, PhRvD, 73, 103002

Davis, T. M., Hui, L., Frieman, J. A., et al. 2011, ApJ, 741, 67

De Bernardis, F., Aiola, S., Vavagiakis, E. M., et al. 2017, JCAP, 3, 008

DeDeo, S., Spergel, D. N., & Trac, H. 2005, arXiv Astrophysics e-prints, astro-ph/0511060

Deutsch, A.-S., Dimastrogiovanni, E., Johnson, M. C., Münchmeyer, M., & Terrana, A. 2018, PhRvD, 98, 123501

Fisher, K. B., Lahav, O., Hoffman, Y., Lynden-Bell, D., & Zaroubi, S. 1995, MNRAS, 272, 885

Hada, R., & Eisenstein, D. J. 2018, MNRAS, 478, 1866

—. 2019, MNRAS, 482, 5685

Hand, N., Addison, G. E., Aubourg, E., et al. 2012, Physical Review Letters, 109, 041101

Harnois-Déraps, J., Pen, U.-L., Iliev, I. T., et al. 2013, MNRAS, 436, 540

Ho, S., Dedeo, S., & Spergel, D. 2009, arXiv e-prints, arXiv:0903.2845
Hui, L., & Greene, P. B. 2006, PhRvD, 73, 123526
Li, M., Angulo, R. E., White, S. D. M., & Jasche, J. 2014, MNRAS, 443, 2311
Li, Y.-C., Ma, Y.-Z., Remazeilles, M., & Moodley, K. 2018, PhRvD, 97, 023514
McCarthy, F., & Johnson, M. C. 2019, arXiv e-prints, arXiv:1907.06678
Modi, C., Feng, Y., & Seljak, U. 2018, Journal of Cosmology and Astro-Particle Physics, 2018, 028
Münchmeyer, M., Madhavacheril, M. S., Ferraro, S., Johnson, M. C., & Smith, K. M. 2018, arXiv e-prints, arXiv:1810.13424
Nusser, A., & Davis, M. 1994, ApJL, 421, L1
Pan, Z., & Johnson, M. C. 2019, arXiv e-prints, arXiv:1906.04208
Planck Collaboration, Ade, P. A. R., Aghanim, N., et al. 2016, A&A, 586, A140
Schmidt, F., Elsner, F., Jasche, J., Nguyen, N. M., & Lavaux, G. 2019, JCAP, 1, 042
Schmittfull, M., Baldauf, T., & Zaldarriaga, M. 2017, PhRvD, 96, 023505
Schmittfull, M., Simonović, M., Assassi, V., & Zaldarriaga, M. 2018, arXiv e-prints, arXiv:1811.10640
Seljak, U., Aslanyan, G., Feng, Y., & Modi, C. 2017, Journal of Cosmology and Astro-Particle Physics, 2017, 009
Shao, J., Zhang, P., Lin, W., Jing, Y., & Pan, J. 2011, MNRAS, 413, 628
Shi, F., Yang, X., Wang, H., et al. 2016, ApJ, 833, 241
Shi, Y., Cautun, M., & Li, B. 2018, PhRvD, 97, 023505
Smith, K. M., Madhavacheril, M. S., Münchmeyer, M., et al. 2018, arXiv e-prints, arXiv:1810.13423
Wang, H., Mo, H. J., Yang, X., Jing, Y. P., & Lin, W. P. 2014, ApJ, 794, 94
Wang, X., & Pen, U.-L. 2019, ApJ, 870, 116
Yu, H.-R., Yu, Y., Motloch, P., et al. 2019, arXiv e-prints, arXiv:1904.01029
Yu, Y., Zhu, H.-M., & Pen, U.-L. 2017, ApJ, 847, 110
Zhang, P., Zheng, Y., & Jing, Y. 2015, PhRvD, 91, 043522
Zheng, Y., Zhang, P., & Jing, Y. 2015, PhRvD, 91, 043523
Zheng, Y., Zhang, P., Jing, Y., Lin, W., & Pan, J. 2013, PhRvD, 88, 103510
Zhu, H.-M., & Castorina, E. 2019, arXiv e-prints, arXiv:1905.00361
Zhu, H.-M., Yu, Y., & Pen, U.-L. 2018, PhRvD, 97, 043502
Zhu, H.-M., Yu, Y., Pen, U.-L., Chen, X., & Yu, H.-R. 2017, PhRvD, 96, 123502